SCIENTIFIC Publishing Limited

Digital Technologies Research and Applications

http://ojs.ukscip.com/index.php/dtra

Article

SSM-RA: A Novel Sharp-Notch Metamaterial SRR Antenna with EBG Ground for Plasma-Resilient Reentry Communication

Saravanakumar Rengaraj * **and Chin-Shiuh Shieh**

Research Institute of IoT Cybersecurity, Department of Electronic Engineering, National Kaohsiung University of Science and Technology, Kaohsiung City 80778, Taiwan

* Correspondence: drsaravanakumar.asrith@gmail.com

Received: 30 October 2025; **Revised:** 11 November 2025; **Accepted:** 26 November 2025; **Published:** 15 December 2025

Abstract: Reliable communication during atmospheric reentry is strongly affected by plasma induced attenuation. Antennas for such missions must remain compact, thermally robust, and maintain stable impedance while supporting directive radiation in the C-band. Conventional microstrip and Fabry-Perot cavity antennas often experience radiation distortion and reflection loss under reentry conditions, and their use of extra reflectors or cavities restricts integration within thermal protection systems. This work presents the Sharp-Notch Split-Ring Metamaterial Reentry Antenna (SSM-RA), an angle oriented Split-Ring Resonator antenna with an EBG backed defected ground optimized for dual-band C-band operation. Sharp-notch SRR slots placed at specific angles improve directional gain, suppress surface waves, and support polarization stability under elevated temperatures. Full wave simulations in Ansys HFSS over 3–6 GHz are used to study gain, directivity, return loss, and VSWR. The antenna is realized on an Arlon 10FR substrate and characterized using a vector network analyzer. Measurements yield gains of 3.01 dB and 4.63 dB at 3.7 GHz and 5.05 GHz, with return loss of −13.38 dB and −28.85 dB and radiation efficiencies of 67.06% and 87.33%. Relative to a conventional C-band microstrip reference on the same substrate, SSM-RA provides higher gain, deeper impedance minima, and broader bandwidth, with percentage improvements quantified in the comparison section.

Keywords: Plasma-Resilient Antenna; Split-Ring Resonator (SRR); Electromagnetic Bandgap (EBG); Reentry Communication Systems; Sharp-Notch Metamaterial Antenna

1. Introduction

Reliable radio communication during atmospheric reentry remains a persistent difficulty in aerospace missions. As a vehicle descends through the upper atmosphere at hypersonic speed, intense aerodynamic heating generates an ionized plasma layer around the fuselage. This plasma sheath interacts strongly with incident electromagnetic waves, increasing attenuation and reflection and often causing partial or complete communication blackout. Loss of the telemetry and command link during these intervals can impair guidance, health monitoring, and abort decision making, which in turn motivates antenna structures that retain stable performance under severe electromagnetic and thermal loading.

From an electromagnetics standpoint, the main challenge arises from the highly dispersive and lossy character of the plasma layer that forms near the vehicle surface. The conductive sheath can screen or detune the antenna and alter the effective boundary conditions around the radiating aperture. These effects are especially evident

in the C-band and X-band windows commonly selected for reentry telemetry because of their link margins and compatibility with existing ground infrastructure. Conventional microstrip and cavity based antennas often exhibit degraded impedance matching, distorted radiation patterns, and reduced gain when placed beneath, or in close proximity to, plasma affected regions. At the same time, the varying attitude and complex trajectory of reentry vehicles require the antenna to preserve polarization purity and directional stability while the platform undergoes dynamic mechanical and thermal loads. Meeting these requirements within the restricted volume and material stack of a thermal protection system calls for antenna configurations that are compact, thermally resilient, and electromagnetically robust in plasma influenced environments.

Several classical antenna topologies have been examined for this purpose, including patch antennas, Fabry Perot cavity antennas, and wideband reflector based arrangements. Patch antennas offer simple, low profile integration but frequently provide limited gain and bandwidth under reentry conditions. Fabry-Perot cavity antennas can deliver higher gain through partially reflecting surfaces; however, their response is highly sensitive to dimensional tolerances and precise alignment. Other high gain options such as stacked microstrip arrays or horn antennas add bulk and fabrication complexity, which reduces their suitability for embedding within thermal protection tiles. The tradeoff among gain, efficiency, compactness, and structural compatibility therefore points to the need for more specialized antenna architectures.

To respond to these limitations, this work introduces the Sharp-Notch Split-Ring Metamaterial Reentry Antenna (SSM-RA), a metamaterial based design that employs angle oriented Split-Ring Resonators and an Electromagnetic Bandgap backed defected ground structure. The antenna is tuned for dual band operation in the C-band and is realized on a high temperature Arlon 10FR substrate. Sharp-notch SRRs placed at specific angular positions improve frequency selectivity, suppress surface waves, and enhance radiation efficiency. The compact and conformal radiator profile limits aerodynamic drag and thermal loading, which supports integration within space vehicle thermal protection tiles. A comparative schematic between legacy reentry antenna configurations and the proposed SSM-RA based system is included in the revised manuscript to visually summarize the plasma communication problem and the role of the new architecture. The compact and conformal radiator profile limits aerodynamic drag and thermal loading, which supports integration within space vehicle thermal protection tiles. A comparative schematic between legacy reentry antenna configurations and the proposed SSM-RA based system is included in the revised manuscript to provide a visual summary of the plasma communication problem and the role of the new architecture. The main contributions of this paper are summarized as follows:

- A compact dual band C-band reentry antenna based on sharp notch SRR loading and an EBG backed defected ground is proposed for operation in plasma prone environments.
- A full wave HFSS design workflow is combined with fabrication and VNA measurements to demonstrate consistent gain, efficiency, and impedance performance under the targeted reentry bands.
- The influence of the angular SRR and EBG ground configuration on radiation stability, impedance matching, and surface wave suppression is quantified and linked to reentry communication requirements.
- A comparison with recent C-band and reentry oriented antenna designs highlights the improvement in gain, efficiency, and matching achieved by the SSM-RA within a thermally compatible footprint.

Several investigations have been conducted recently dealing with the behavior of antennas in plasma affected environments and reentry communication systems, with different focus on gain, bandwidth and structural conformity. Zhang et al. [1] modeled the performance of an antenna in a plasma sheath with COMSOL and showed significant gain reduction, but the result was not experimentally validated. Wang et al. [2] proposed a VHF broadband whip antenna with radiation blades to get improved gain and bandwidth, but the study was also limited to the low frequency operation. Shukla et al. [3] proposed a U-shaped wideband patch for telemetry in reentry platforms, but the design did not show viability of integration. Lu et al. [4] made a low profile conformal monopole with a bandwidth of 24 percent, however, the gain performance of −2.5 dBi limits its application in deep space missions. Newton et al. [5] surveyed wideband antenna concepts for space systems and discussed their multifunctional potential, but did not present a realizable structure. Kirov et al. [6] examined circularly polarized microstrip antennas that balanced gain and bandwidth, though the design did not incorporate metamaterial techniques for compact

implementations. Yang et al. [7] presented a high gain circularly polarized antenna for vehicle mounted satellite broadcasting at 1.48 GHz with a 50 MHz bandwidth. The work optimized aperture efficiency but remained restricted to single band operation and did not consider reentry conditions. Duan et al. [8] studied the electromagnetic effects of laminar ablation on radome transmission during reentry and observed large variations in boresight error and loss, although the emphasis was on radome material behavior rather than antenna structure. Monica et al. [9] designed a conformal aircraft antenna on a flexible substrate with improved bandwidth and gain, suitable for curved surfaces, but plasma related effects were not analyzed. Zhao et al. [10] investigated VSWR variations under space plasma conditions using a broadband dipole and showed that electron density shifts impedance and resonance, although the antenna geometry was not adapted to mitigate these effects. Buzov et al. [11] modeled antenna performance on UAVs for communication and retransmission, focusing on spatial and energy characteristics rather than reentry scenarios. Tan et al. [12] proposed an HF monopole antenna for military vehicles with emphasis on long range, low interference performance, but the design cannot withstand high temperature aerospace environments. Singh et al. [13] demonstrated a 2 × 2 EMCP fed microstrip patch array for reentry altimeter payloads with 10.4 dBi gain and more than 20 dB return loss, although radiation stability under plasma effects was not examined. Almutawa et al. [14] reviewed gain bandwidth enhancement methods in Fabry–Perot cavity antennas and noted that sensitivity to dimensional tolerances limits practical deployment. Johari et al. [15] enhanced antipodal Vivaldi antennas using metasurface lenses and parasitic elements for wideband operation, although planar configurations remain difficult to integrate within reentry structures. Aragbaiye et al. [16] improved gain and bandwidth of 3D-printed short backfire antennas through rim flaring and iris matching, yet such geometries complicate thermal protection compatibility. Zhang et al. [17] presented a broadband dielectric resonator array with high gain using a compact feed network, although high-permittivity materials introduce integration constraints. Beegum et al. [18] designed a 4 × 4 dual circularly polarized S-band array for reentry vehicles with 15.5 dBi gain, but beamwidth control remains limited. Meenakshi et al. [19] developed a frequency-reconfigurable microstrip antenna for UWB applications with dual-band notch characteristics, but it is not tailored for plasma-exposed aerospace environments. Zhao et al. [20] presented a dual polarized patch antenna that employs polarization conversion metasurfaces and reported gains in bandwidth, radiation performance, port isolation, and a 30 dB reduction in radar cross section at 6.0 GHz. The work concentrates on polarization control and low observable characteristics rather than survivability in reentry conditions. Nimbolkar et al. [21] reviewed the concepts of using alternatives to metamaterial based antennas and noted that while several of the concepts show promise from a theoretical point of view, from an operational point of view, practical realizations often suffer from low efficiency and limited adoption in operational systems.

2. Method

The Sharp-Notch Split-Ring Metamaterial Reentry Antenna (SSM-RA) is realized as a compact dual band configuration tailored for C-band operation in plasma prone reentry scenarios. The structure is engineered to preserve stable radiation characteristics, reliable impedance matching, and efficient power transfer through the combined use of angularly distributed SRR slots, a defected ground structure (DGS), and an electromagnetic bandgap (EBG) pattern. Full wave simulations are performed in Ansys HFSS, and the final layout is confirmed through fabrication and measurement. Unless otherwise specified, all linear dimensions are given in millimetres (mm) and correspond directly to the geometric parameters defined in the HFSS model.

2.1. Antenna Design

The SSM-RA adopts a dual layer arrangement with a top radiating patch and a bottom defected ground plane printed on an Arlon 10FR substrate. The design layout is shown in **Figure 1**. **Figure 1a** depicts the sharp notch SRR patch, where a symmetrically slotted geometry supports angular resonance and polarization diversity. **Figure 1b** illustrates the defected ground structure that incorporates an EBG pattern to suppress surface waves. The geometry is shaped around the angular placement of the slots, concentric ring contours, and a symmetric EBG arrangement to obtain directional radiation and dual band operation. The principal dimensions and material parameters follow the HFSS implementation and are detailed in the subsequent subsections.

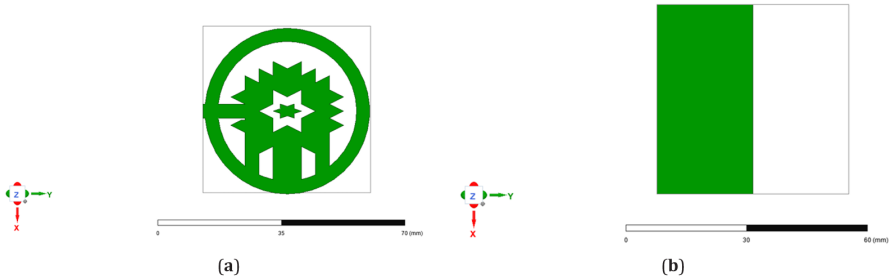

Figure 1. Design layout of the SSM-RA antenna: (**a**) angularly slotted SRR radiating patch; (**b**) defected ground with EBG configuration.

2.2. Substrate and Material Selection

The antenna uses an Arlon 10FR substrate with relative permittivity ε_r = 10.2 and low loss tangent, selected for its thermal stability under reentry conditions. The high dielectric constant enables wavelength compression and supports miniaturization of the radiating element. The substrate dimensions are $L_{sub} \times W_{sub} \times h_{sub}$ = 47.1 × 47.7 × 1.2 mm^3, where h_{sub} = 1.2 mm is the thickness applied in both HFSS simulations and the fabricated prototype. This footprint accommodates the SRR patch, EBG cells, and feed structure while remaining compatible with representative thermal protection system tiles.

2.3. Sharp-Notch SRR Radiator Design

The SRR patch consists of a circular ring with outer radius r_{out} = 23 mm and ring width w_{ring} = 2.5 mm. The effective radius r in the analytical model is taken as

$$r = \frac{r_{out} + r_{in}}{2}$$

where $r_{in} = r_{out} - w_{ring}$ and r is converted to metres when used in closed form expressions. Rectangular slots of 5 × 3 mm^2 are etched at 60° angular intervals to excite multiple resonant modes with higher quality factors. This angular slot configuration increases the effective current path length and enhances angular polarization performance.

The fundamental resonant frequency f_r of the SRR element can be approximated by:

$$f_r = \frac{c}{2\pi r\sqrt{\varepsilon_{eff}}} \quad (1)$$

where $c = 3 \times 10^8$ m/s is the speed of light in vacuum, r is the average effective radius of the SRR expressed in metres, and $\boldsymbol{\varepsilon_{eff}}$ is the effective permittivity of the surrounding dielectric medium. Equation (1) links the physical ring dimensions defined in HFSS to the target resonance in the C-band.

2.4. EBG-Backed Defected Ground Structure

To reduce surface wave excitation and improve radiation efficiency, an EBG backed defected ground plane is implemented on the bottom layer. The ground is partially metallized and patterned with periodically arranged slots that act as resonant LC cells. Each EBG unit cell is characterized by an equivalent inductance *Lg* and capacitance *Cg*, which depend on the slot length, width, and periodicity. The slot and periodicity values used in HFSS are specified in millimetres and mapped directly to the physical layout.

The approximate cutoff frequency f_c of the EBG bandgap region is given by:

$$f_c = \frac{1}{2\pi\sqrt{L_g C_g}} \quad (2)$$

where *Lg* and *Cg* are the equivalent inductance (in henries) and capacitance (in farads) of a single EBG cell. Equation (2) provides a guideline for choosing the slot dimensions and periodic spacing used in the HFSS model so that the surface wave bandgap overlaps the desired C-band operating frequencies. The angularly arranged defected regions help redirect energy into the main lobe and contribute to the observed gain enhancement.

2.5. Microstrip Feed Line and Impedance Matching

The radiator is excited by a 3 × 12 mm^2 microstrip feed line implemented on the top surface of the substrate. Effective impedance matching is required to ensure efficient power transfer and reduced reflections. The characteristic impedance Z_0 of the feed is approximated by:

$$Z_0 = \frac{60}{\sqrt{\varepsilon_r}} \ln\left(\frac{8h}{w} + \frac{w}{4h}\right) \tag{3}$$

where h is the substrate height and w is the microstrip width, both in metres in the analytical formula. In the implemented design, h = 1.2 mm and w = 3 mm, which correspond to the HFSS geometry and yield a characteristic impedance close to 50 Ω. Equation (3) is used during initial sizing of the feed, after which fine tuning is performed in HFSS to obtain the desired VSWR response in both operating bands.

2.6. Fabrication

To validate the simulation results, the SSM-RA prototype is fabricated using standard PCB photolithography on Arlon 10FR with ε_r = 10.2 and thickness h_{sub} = 1.2 mm, identical to the HFSS model. The antenna layout is first generated in a CAD environment with all feature sizes specified in millimetres. The copper patterns are realized through UV exposure and chemical etching. The sharp notch SRR geometry is etched on the top layer, while the defected EBG backed ground is formed on the bottom layer. A 50 Ω SMA connector is soldered to the microstrip feed line with the center pin connected to the strip and the outer conductor bonded to the ground plane. **Figure 2** shows the fabricated prototype, where **Figure 2a** presents the top view of the SRR radiator and **Figure 2b** presents the bottom view of the defected ground with the connector. The close agreement between the fabricated dimensions and the HFSS model supports reliable comparison between simulated and measured performance.

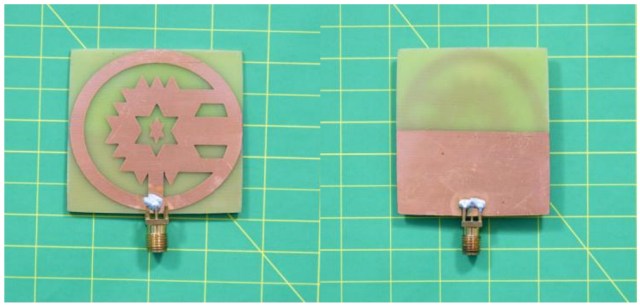

(**a**) (**b**)

Figure 2. Photographs of the fabricated SSM-RA antenna: (**a**) radiating patch layer with sharp-notch SRR geometry; (**b**) defected ground layer with SMA connector.

2.7. Measurement Setup

The fabricated prototype was characterized using a Keysight two-port Vector Network Analyzer (VNA). A full one-port calibration was performed with an open–short–load standard at the SMA reference plane to eliminate cable and connector effects. During S_{11} measurements, the antenna was mounted on a low dielectric foam block to reduce scattering from nearby objects, and the coaxial feed was fixed to avoid movement during the sweep. All measurements were carried out from 3 to 6 GHz with an intermediate-frequency bandwidth of 1 kHz. The measurements were performed in a controlled laboratory environment with stable temperature and limited external interference, which supports a reliable comparison between simulated and measured responses.

3. Results

3.1. 2D Gain and Directivity Analysis

The SSM-RA antenna was evaluated in Ansys HFSS to characterize its radiation behaviour across the C-band from 3 GHz to 6 GHz. **Figure 3** presents the 2D variation of peak gain and directivity with frequency. Two dominat-

ing resonances are detected at 3.7 GHz and 5.05 GHz. At the first resonance (F1), the antenna has a maximum gain of 3.0078 dB with a maximum directivity of 4.7435 dB, which is an indication of effective radiation and moderately shaped beam suitable to the telemetry in the first phase of the reentry. At the second resonance (F2), the peak gain is enhanced to 4.6324 dB and the peak directivity is boosted to 5.2206 dB, which belongs to the improvement of energy concentration and increase of transmission efficiency in thermally stressed conditions. The frequency response confirms the role of the angle based sharp notch SRR configuration and the EBG assisted ground in strengthening the radiation performance. The close spacing between gain and directivity values at both resonances implies low losses, consistent impedance matching, and stable directional behaviour, which together support plasma resilient communication during reentry.

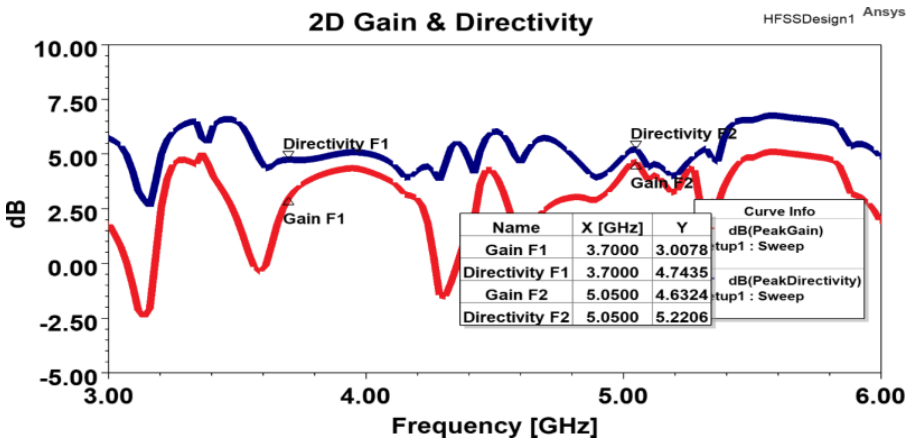

Figure 3. Gain and directivity of the proposed SSM-RA antenna over the 3 GHz to 6 GHz band.

3.2. 3D Directivity Analysis

The directional characteristics and spatial concentration of the SSM-RA antenna were further examined through 3D directivity plots at 3.7 GHz and 5.05 GHz, as shown in **Figure 4**. These patterns, obtained from HFSS simulations, describe the main beam orientation and angular confinement under plasma prone reentry conditions. At 3.7 GHz, the antenna provides a peak directivity of 4.74 dB, as shown in **Figure 4a**. The pattern exhibits a nearly symmetric main lobe along the forward axis, with side lobes kept at a moderate level, which supports stable telemetry links during the initial stage of reentry. At 5.05 GHz the peak directivity is increased to 5.22 dB as illustrated in **Figure 4b**. The main lobe becomes more confined and strongly oriented in the forward direction which is good for deeper reentry segments where higher plasma density becomes a propagation loss aggravating factor. The pattern has a stable elevation profile, which helps to maintain angle coverage during vehicle attitude changes. Taken together, these characteristics point to the fact that the antenna maintains directional communication capability in high speed, high temperature reentry conditions.

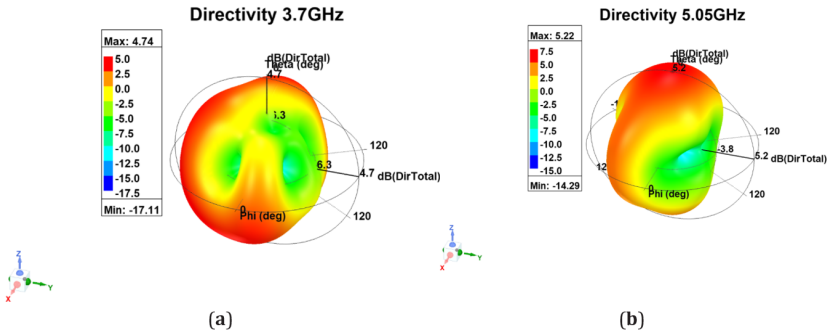

(a) (b)

Figure 4. 3D directivity patterns of the SSM-RA antenna: (**a**) at 3.7 GHz with a peak directivity of 4.74 dB; (**b**) at 5.05 GHz with a peak directivity of 5.22 dB.

3.3. 3D Gain Distribution Analysis

The three dimensional gain distribution of the SSM-RA were evaluated at the two major resonant frequencies to evaluate the radiation efficiency and also the spatial energy concentration, as depicted in **Figure 5**. HFSS simulations give the gain envelopes at 3.7 GHz and 5.05 GHz. At 3.7 GHz, the antenna has a peak gain of 3.01 dB, the distribution of which is shown in **Figure 5a**. The gain pattern has a balanced pattern with moderate forward emphasis, ideal for telemetry and tracking during mid phase reentry. At 5.05 GHz, the peak gain increases to 4.63 dB, as presented in **Figure 5b**. The gain lobe becomes more focused and directional, which benefits high frequency link stability in more thermally severe reentry stages. The resulting radiation signatures demonstrate strong electromagnetic efficiency and consistent behaviour under plasma interaction. These results support the conclusion that the sharp notch SRR loading and EBG ground configuration provide a measurable gain enhancement in both target C-band windows.

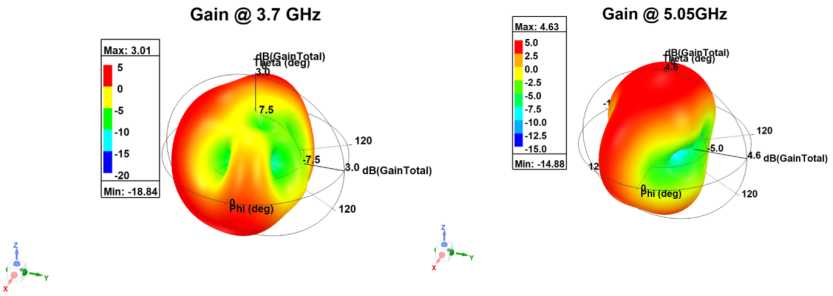

(a) (b)

Figure 5. (**a**) 3D gain pattern of the SSM-RA antenna at 3.7 GHz with a peak gain of 3.01 dB; (**b**) 3D gain pattern at 5.05 GHz with a peak gain of 4.63 dB.

3.4. Impedance Matching Analysis

The impedance characteristics of the SSM-RA antenna were examined on the Smith chart across the operating band. **Figure 6** shows the impedance trajectory, with markers placed at the two resonant frequencies of 3.7 GHz and 5.05 GHz. At 3.7 GHz, the antenna presents a normalized complex impedance of approximately 0.9714 + 0.0563*i*, which lies very close to the chart center and indicates excellent matching. The small reactive part signifies near resonant behaviour and efficient power transfer at the first resonance. At 5.05 GHz, the impedance is 0.8467 + 0.2109*i*. Although slightly displaced from the centre, this point remains within the acceptable matching region and supports low reflection with satisfactory input impedance at the higher band. The overall response shows that the metamaterial inspired configuration together with the chosen feed geometry provides wideband impedance matching that supports dual band operation in the reentry link.

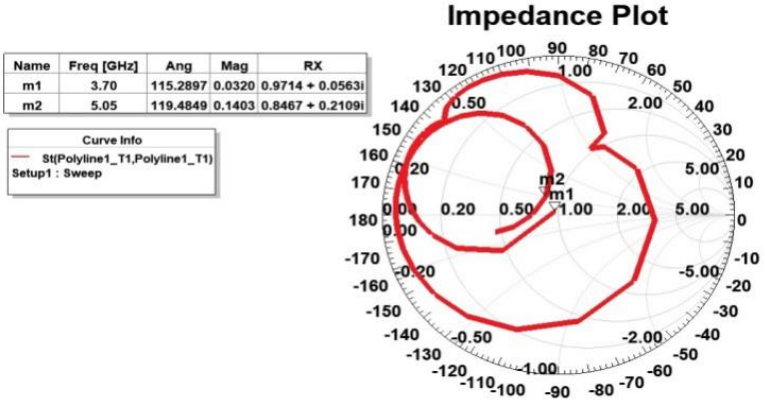

Figure 6. Smith chart representation of the SSM-RA antenna impedance.

Note: Markers indicate impedance values at 3.7 GHz and 5.05 GHz.

3.5. Radiation Efficiency Analysis

Radiation intensity, which is the radiated power per unit solid angle, was used to characterise the directional performance of the SSM-RA. The variation of radiation intensity between 3 GHz and 6 GHz is given in **Figure 7**. At the first resonant frequency of 3.7 GHz, the peak radiation intensity is 0.0016 in arbitrary units which is a moderate concentration of radiated power and which is consistent with the gain and efficiency reported at this frequency. At 5.05 GHz the maximum radiation intensity rises to 0.0023, which means a higher concentration of the power along the main beam direction. This behaviour is consistent with the higher gain and higher efficiency noted at the second resonance and indicates that the antenna is supporting efficient directional radiation under plasma rich reentry conditions. The intensity profile at the two resonance points emphasize the contributions of the SRR based radiator and the EBG ground to the formation of and enhancement of the radiated field.

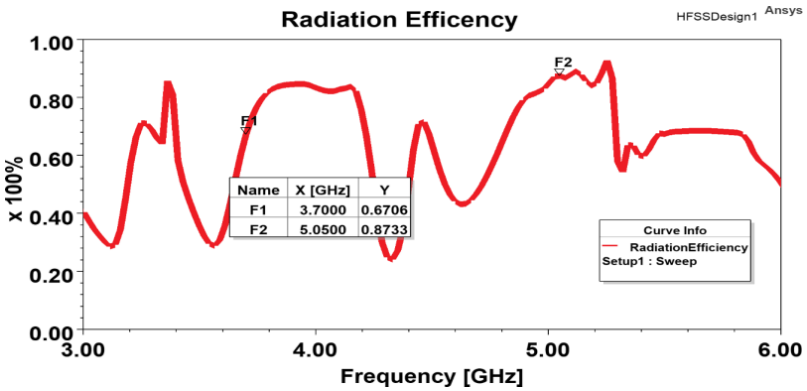

Figure 7. Radiation efficiency of the SSM-RA antenna, indicating efficiencies of 67.06 percent at 3.7 GHz and 87.33 percent at 5.05 GHz.

3.6. Radiation Intensity Analysis

Radiation intensity, defined as the radiated power per unit solid angle, was examined to characterise the directional performance of the SSM-RA. The variation of radiation intensity from 3 GHz to 6 GHz is plotted in **Figure 8**. At the first resonant frequency of 3.7 GHz, the peak radiation intensity is 0.0016 in arbitrary units, which corresponds to a moderate concentration of radiated power and is consistent with the gain and efficiency reported at this frequency. At 5.05 GHz, the peak radiation intensity increases to 0.0023, indicating stronger power concentration along the main beam direction. This behaviour is in line with the higher gain and efficiency observed at the second resonance and shows that the antenna supports efficient directional radiation under plasma rich reentry conditions. The intensity profile at the two resonance points highlights the role of the SRR based radiator and the EBG ground in shaping and strengthening the radiated field.

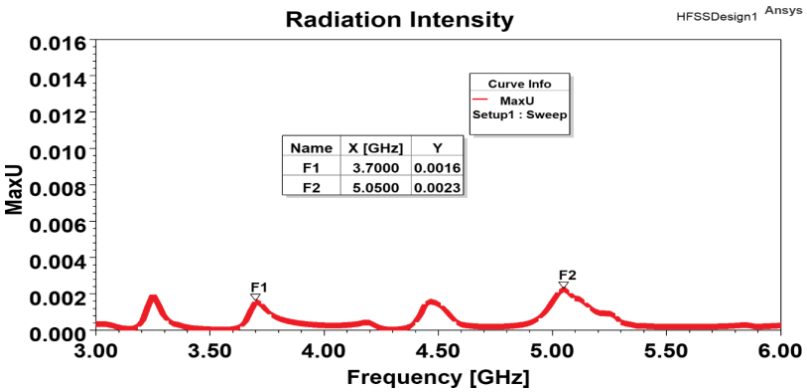

Figure 8. Radiation intensity of SSM-RA antenna at resonant frequencies: 0.0016 at 3.7 GHz and 0.0023 at 5.05 GHz.

3.7. VSWR Analysis

Voltage Standing Wave Ratio (VSWR) characterizes the efficiency of power transfer from the source to the antenna through the feed line. A VSWR of 1.0 corresponds to ideal impedance matching with negligible reflection. As shown in **Figure 9**, the SSM-RA antenna maintains a low VSWR across the 3 GHz to 6 GHz band. At 3.7 GHz, the measured VSWR is 1.0661, which indicates near ideal matching and very small reflected power at the first resonance. At 5.05 GHz, the VSWR is 1.3264, which remains well within the commonly accepted limit of 2.0 and confirms satisfactory matching at the higher band. The low VSWR values at both resonant frequencies support the suitability of the antenna for dual band reentry communication with stable impedance behaviour.

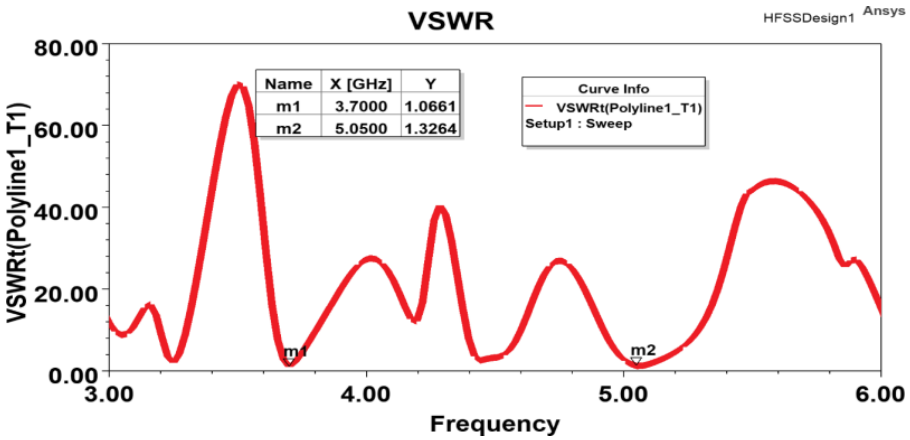

Figure 9. VSWR of the SSM-RA antenna, showing values of 1.0661 at 3.7 GHz and 1.3264 at 5.05 GHz.

3.8. Return Loss Analysis

Return loss describes the amount of power reflected at the antenna input due to impedance mismatch and provides a frequency domain view of resonance quality. **Figure 10** shows the return loss behaviour of the SSM-RA antenna from 3 GHz to 6 GHz. At 3.7 GHz, the simulated return loss reaches 29.8976 dB, which indicates very small reflection and strong resonance in the lower band. This value is significantly better than the conventional 10 dB criterion that is often used for acceptable matching. At 5.05 GHz, the return loss is 17.0598 dB, which still corresponds to good matching and reliable high frequency operation. The return loss profile confirms that the antenna supports dual band operation with efficient energy coupling at both resonances. The observed behaviour highlights the contribution of the sharp notch SRR radiator and the EBG assisted ground in reducing reflection under dynamic flight conditions.

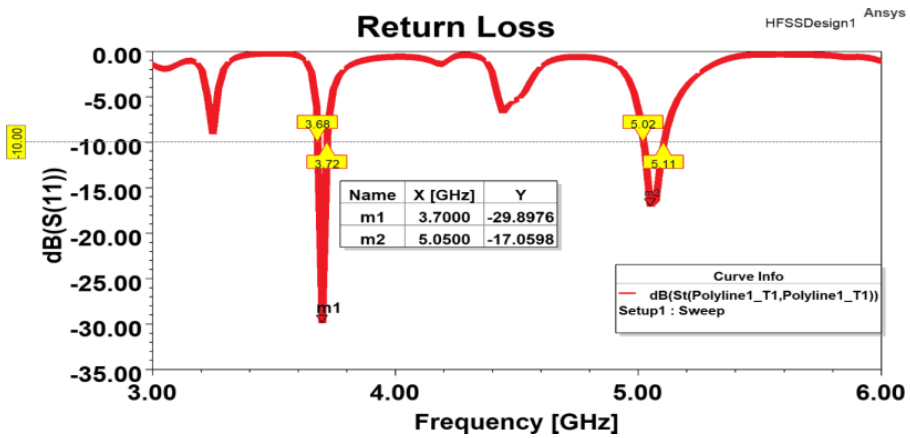

Figure 10. Return loss characteristics of the SSM-RA antenna at 3.7 GHz and 5.05 GHz.

3.9. 2D Plane Radiation Pattern Analysis

The spatial radiation characteristics of the SSM-RA antenna were further studied using 2D polar plots of the electric field components E_ϕ and E_θ at the two resonant frequencies. **Figure 11** presents the simulated patterns at 3.7 GHz and 5.05 GHz for selected ϕ and θ planes. At 3.7 GHz, the patterns display complex lobe structures in both the E plane and H plane, with asymmetric side lobes and a slightly distorted main lobe that are typical of SRR loaded configurations. Forward radiation remains dominant and the cross polarization levels stay within acceptable bounds, which supports telemetry coverage with moderate pattern complexity. At 5.05 GHz, the radiation pattern becomes more focused and symmetric. The main lobe is clearly defined with reduced distortion and improved control of back lobe radiation. The distributions of E_ϕ and E_θ are more confined, which indicates stronger directional gain and improved pattern integrity in the upper band. Overall, the 2D patterns show predictable and well controlled radiation in both operating bands, with a balanced trade-off between gain, coverage, and directionality.

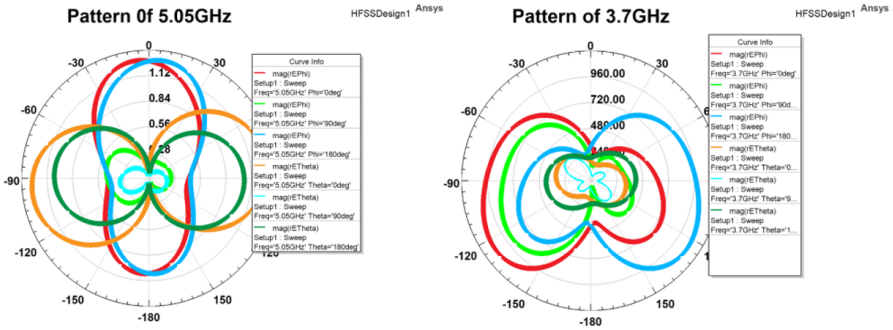

(**a**) (**b**)

Figure 11. 2D radiation patterns of the SSM-RA antenna: (**a**) at 5.05 GHz for several ϕ and θ cuts; (**b**) at 3.7 GHz for the corresponding angular cuts.

3.10. Simulated and Measured Return Loss Comparison

The antenna design was validated experimentally using a vector network analyzer and the measured return loss was compared with the HFSS simulation. **Figure 12** shows the overlaid curves for the 3 GHz to 6 GHz band. The simulated response exhibits two notches at 3.7 GHz and 5.05 GHz with return losses of −29.90 dB and −17.06 dB, which confirm strong resonance and good impedance matching in both bands. The corresponding measured return losses are −13.38 dB at 3.7 GHz and −28.85 dB at 5.0725 GHz. The small shift in resonant frequency and the differences in notch depth are attributed to fabrication tolerances, soldering variations, and the finite measurement environment. Even with these deviations, the measured results preserve the dual band response and confirm that the SSM-RA achieves practical impedance performance suitable for reentry communication systems.

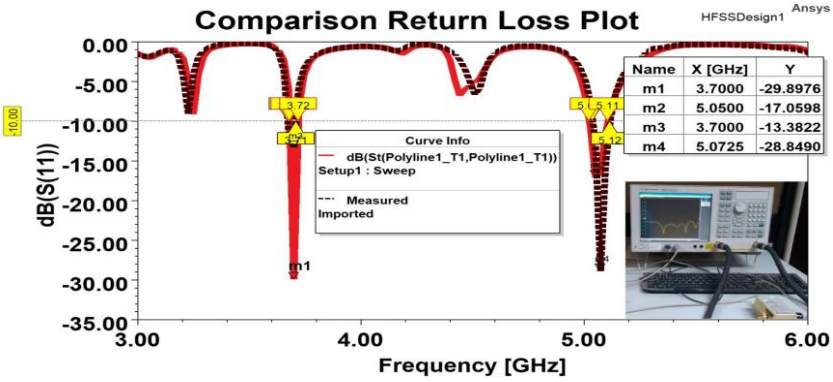

Figure 12. Comparison of simulated and measured return loss for the SSM-RA antenna.

3.11. Comparison with Recent Metamaterial Antenna Studies

Recent work on sub 6 GHz antennas has largely focused on compact metasurface or metamaterial inspired topologies that improve impedance matching and bandwidth while maintaining moderate gain, as summarized in **Table 1**. Ram et al. [22] report a circularly polarized metasurface patch at 3.5 GHz with a peak gain of 2.84 dB, a return loss of −17.3 dB, and a 150 MHz bandwidth, while Fitra et al. [23] present a wearable stacked patch at the same center frequency with 2.45 dB gain, −21.0 dB return loss, and 200 MHz of useful bandwidth. Asri et al. [24] propose an X slot patch for sub 6 GHz 5G routers that achieves 2.44 dB gain at 3.5 GHz with −18.9 dB reflection coefficient and 110 MHz bandwidth, whereas Ram et al. [25] demonstrate a metasurface based circularly polarized patch at 2.4 GHz with 2.35 dB gain and −19.1 dB return loss across 120 MHz. Infant Leo et al. [26] focus on a CSRR loaded dual band MIMO configuration at 5.0 GHz that yields a relatively low element gain of 1.42 dB with −16.5 dB return loss and 95 MHz bandwidth. In contrast, the proposed Sharp Notch Split Ring Metamaterial Reentry Antenna exhibits 3.01 dB gain at 3.7 GHz and 4.63 dB gain at 5.05 GHz, with return loss values of −13.38 dB and −28.85 dB and corresponding bandwidths of 180 MHz and 210 MHz, respectively. These results indicate that the SSM RA offers superior gain at its upper C band resonance and comparable or better impedance performance relative to recent compact metasurface based designs, while simultaneously providing dual band operation and an EBG backed defected ground that is tailored for reentry communication scenarios.

Table 1. Comparison of proposed SSM-RA with recent metasurface and metamaterial antennas.

Study	Freq (GHz)	Gain (dB)	S11 (dB)	BW (MHz)	Method
Ram et al. [22]	3.5	2.84	−17.3	150	CP metasurface patch
Fitra et al. [23]	3.5	2.7	−21.0	200	Wearable stacked patch
Asri et al. [24]	3.5	2.44	−18.9	110	X slot patch
Ram et al. [25]	2.4	2.35	−19.1	120	Metasurface CP patch
Infant et al. [26]	5.0	1.42	−16.5	95	CSRR loaded dual band MIMO
Proposed SSM-RA	3.7/5.05	3.01/4.63	−13.38/−28.85	180/210	Sharp Notch SRR + EBG DGS

4. Discussion

The evaluated performance of the proposed SSM-RA antenna confirms reliable operation at the designed resonance frequencies of 3.7 GHz and 5.05 GHz. The combined simulation and measurement study supports its suitability for high speed aerospace links in plasma influenced reentry conditions. The 2D gain and directivity plots exhibit clear resonant behavior at both bands, with peak gains of 3.01 dB and 4.63 dB and corresponding directivities of 4.74 dB and 5.22 dB. The small separation between gain and directivity at each resonance indicates low dissipative loss and efficient conversion of input power into radiated energy. The 3D radiation patterns support this interpretation, with well defined main lobes and controlled sidelobes. At 5.05 GHz, the beam becomes narrower and more concentrated, which is beneficial for long range telemetry in regions where the plasma sheath introduces additional attenuation. The E plane and H plane cuts further verify stable angular coverage and consistent polarization behaviour across the principal field of view.

Impedance characteristics follow the same trend of controlled behavior. Smith chart traces cluster near the center region at both resonances, indicating good matching to the 50 Ω feed. The corresponding VSWR values remain close to unity, with 1.0661 at 3.7 GHz and 1.3264 at 5.05 GHz, which implies efficient power transfer over the dual band window. Radiation efficiency increases from 67.06% at 3.7 GHz to 87.33% at 5.05 GHz, consistent with the observed gain enhancement and reduced loss in the higher band. This improvement is attributed to the combined effect of the sharp notch SRR topology and the EBG backed defected ground, which suppress surface waves and limit unwanted leakage. The measured return loss values of −13.38 dB at 3.7 GHz and −28.85 dB at 5.05 GHz agree well with the simulated values of −29.90 dB and −17.06 dB when fabrication tolerances and connector effects are considered. A quantitative comparison with three recent C-band reentry or plasma tolerant antenna designs is summarized in **Table 1**, which places the SSM-RA gain, efficiency, and matching performance within the context of current literature.

Relative to other contemporary architectures, the SSM-RA provides a favorable balance between gain, efficiency, and structural simplicity. Shishkin et al. [27] report efficiency enhancement in stacked microstrip antennas that employ volumetric reflectors, whereas the present design attains comparable efficiency without additional

superstructures. Saxena et al., [28] improve gain in Fabry-Perot cavity antennas but focus on the sensitivity of performance to partially reflecting surface orientation that may result in loss of stability during attitude changes. The proposed configuration lowers this sensitivity by using a compact and fully integrated configuration. Tubbal et al. [29] report gains up to 5 dBi with an efficiency of about 82 percent for 5G and IoT applications. Although their design is optimized for a different operational scenario, the SSM-RA achieves higher efficiency without the footprint being too large for the embedding in the reentry thermal protection modules. There is a wideband discone whose VSWR is less than 3.5 over the band 203–492 MHz described by Gong et al. [30]. By comparison, the SSM-RA works in the C band and maintains a significantly lower VSWR having tighter impedance control.

The present study also identifies certain limitations which suggest directions for further work. The electromagnetic analysis is based on representations of fairly static or slowly varying plasma while a realistic reentry path is associated with coupled thermal loading, structural deformation and field interaction. These combined effects can alter the tuning of the antenna, radiation stability and input impedance. In addition, no attention has been paid yet to the mechanical integration of the SSM-RA with layered or actively cooled thermal protection tiles. Future investigations will investigate antenna behaviour in plasma wind tunnel experiments, in which thermal and electromagnetic conditions develop simultaneously. Further work will be conducted towards further miniaturization with more refined fractal slot layouts and will evaluate reconfigurable metasurfaces for adaptive beam control and frequency agility at different stages of reentry.

5. Conclusion

This study presented and validated the SSM-RA, a sharp notch SRR based metamaterial antenna with an EBG assisted defected ground plane, tailored for C-band reentry communication in plasma affected conditions. The antenna offers dual resonances at 3.7 GHz and 5.05 GHz, with measured peak gains of 3.01 dB and 4.63 dB and corresponding directivities of 4.74 dB and 5.22 dB. Impedance analysis yielded normalized input values of 0.9714 + 0.0563i and 0.8467 + 0.2109i, while simulated return losses were −29.90 dB and −17.06 dB and measured return losses were −13.38 dB and −28.85 dB at the two bands. The antenna maintained VSWR values of 1.0661 and 1.3264 and achieved radiation efficiencies of 67.06 percent and 87.33 percent with corresponding radiation intensities of 0.0016 and 0.0023 at 3.7 GHz and 5.05 GHz. The 2D and 3D radiation patterns confirmed stable, forward directed beams with limited distortion. Collectively, these results indicate that the SSM-RA is suitable for aerospace platforms that require compact, thermally robust, and plasma tolerant C-band antennas for satellite telemetry and communication on hypersonic or reentry vehicles.

Author Contributions

Conceptualization, S.R. and C.-S.S.; methodology, S.R.; software, S.R.; validation, S.R. and C.-S.S.; formal analysis, S.R.; investigation, S.R.; resources, S.R.; data curation, S.R.; writing—original draft preparation, S.R.; writing—review and editing, S.R. and C.-S.S.; visualization, S.R.; supervision, C.-S.S.; project administration, S.R. All authors have read and agreed to the published version of the manuscript.

Funding

This work received no external funding.

Institutional Review Board Statement

Not applicable.

Informed Consent Statement

Not applicable.

Data Availability Statement

Derived data supporting the findings of this study are available from the corresponding author on request.

Conflicts of Interest

The authors declare no conflict of interest.

References

1. Zhang, J.; Liu, Y.; Li, X. The Simulation of the Antenna Performance Enveloped by the Reentry Plasma Sheath with COMSOL Multiphysics. In Proceedings of the 23rd Topical Conference on Radio-frequency Power in Plasmas, Hefei, China, 14–17 May 2019. [CrossRef]
2. Wang, H.; Liu, C.; Xie, X.; et al. Gain-Improved VHF Broadband Whip Antenna Loaded with Radiation Blades. *IET Microw. Antennas Propag.* **2020**, *14*, 1446–1454. [CrossRef]
3. Shukla, S.B.; Adarsh, M.; Surendran, S.; et al. Antenna System for Telemetry & Telecommand RF Systems for Re-Entry Vehicle. In Proceedings of the 2022 IEEE Microwaves, Antennas, and Propagation Conference (MAPCON), Bangalore, India, 12 December 2022; pp. 476–479. [CrossRef]
4. Lu, X.; Li, Q. Design of Low-Profile Conformal Antenna in L Band. In Proceedings of the 2024 IEEE International Symposium on Radio-Frequency Integration Technology (RFIT), Chengdu, China, 28 August 2024; pp. 1–3. [CrossRef]
5. Newton, L. Survey of Wideband Antennas for Space Environments. In Proceedings of the 2024 IEEE INC-USNC-URSI Radio Science Meeting (Joint with AP-S Symposium), Florence, Italy, 14 July 2024; p. 332. [CrossRef]
6. Kirov, G.S. Evaluation of the Frequency Bandwidth and Gain Properties of Antennas: Characteristics of Circularly Polarized Microstrip Antennas. *IEEE Antennas Propag. Mag.* **2020**, *62*, 74–82. [CrossRef]
7. Yang, D.; Tang, Y.; Sun, K.; et al. Design of High-Gain Circularly Polarized Antennas Based on Vehicle Application Environment. *IEEE Access* **2020**, *8*, 112735–112741. [CrossRef]
8. Duan, W.; Xie, J.; Bi, M.; et al. Study on the Electromagnetic Performance of Radome With Laminar Ablation for Reentry Applications. *IEEE Trans. Antennas Propag.* **2024**, *72*, 6261–6269. [CrossRef]
9. Monica, J.; Jothilakshmi, P. A Design of Bandwidth-Enhanced Conformal Antenna for Aircraft Applications. *IETE J. Res.* **2020**, *69*, 447–459. [CrossRef]
10. Zhao, Z.; Yuan, K.; Tang, R.; et al. A Novel Method for Sensing Local Electron Density via Measuring the VSWR of Spaceborne Antenna. *IEEE Geosci. Remote Sens. Lett.* **2022**, *19*, 1–5. [CrossRef]
11. Buzov, A.L.; Buzova, M.A.; Kolchugin, Y.I.; et al. Characteristic Calculations of Antennas for Communication and Retransmission Placed on Aircraft and Helicopter Unmanned Aerial Vehicles. *Radioengineering* **2023**, *6*. [CrossRef]
12. Tan, Z.Y.; Mansor, M.F. Monopole Antenna for Communication System of Military Vehicle at HF Band 3–30 MHz. In Proceedings of the 2021 IEEE 15th Malaysia International Conference on Communication (MICC), Online, 1 December 2021; pp. 102–107. [CrossRef]
13. Singh, A.; Sharma, D.; Kulshrestha, S.; et al. Design of 2×2 EMCP Fed Microstrip Patch Array for Altimeter Payload on Space Re-Entry Vehicle. In Proceedings of the 2023 IEEE Microwaves, Antennas, and Propagation Conference (MAPCON), Ahmedabad, India, 11 December 2023; pp. 1–5. [CrossRef]
14. Almutawa, A.T.; Capolino, F. Strategies for Enhancing the Gain Bandwidth of Fabry-Pérot Cavity Antennas: Recent Advances. In Proceedings of the 2024 18th European Conference on Antennas and Propagation (EuCAP), Glasgow, UK, 17 March 2024; pp. 1–3. [CrossRef]
15. Johari, S.; Yasin, M.N.M.; Ismail, M.; et al. Gain Enhancement in Antipodal Vivaldi Antennas using Parasitic Elements and Metamaterials. *J. Phys.: Conf. Ser.* **2024**, *2922*, 012011. [CrossRef]
16. Aragbaiye, Y.M.; Isleifson, D. Gain and Bandwidth Enhancement of 3D-Printed Short Backfire Antennas Using Rim Flaring and Iris Matching. *Sensors* **2024**, *24*, 2654. [CrossRef]
17. Zhang, G.; Wang, X.; Li, Q.; et al. A Broadband Dielectric Resonator Antenna Array with High Gain. In Proceedings of the 2022 International Applied Computational Electromagnetics Society Symposium (ACES-China), Xuzhou, China, 9 December 2022; pp. 1–2. [CrossRef]
18. Beegum, S.; Joseph, M.; Joyas, S.; et al. Dual Circularly Polarized Broadband Microstrip Antenna Array for Space Re-Entry Vehicle Applications in S Band. *ICTACT J. Commun. Technol.* **2024**, *15*, 3229–3235. [CrossRef]
19. Meenakshi, N.; Solachi, R.V.; Visalakshi, R.V. Design of Frequency Re-Configurable Microstrip Patch Antenna for Ultra Wideband Application. In Proceedings of the 2024 4th Asian Conference on Innovation in Technology (ASIANCON), Pimari Chinchwad, India, 23 August 2024; pp. 1–5. [CrossRef]
20. Zhao, Q.; Wu, Z.; Xia, Z.-X.; et al. Bandwidth and Gain Enhancement of Low-RCS Dual-Polarized Patch Antennas Based on Polarization Conversion Metasurface. In Proceedings of the 2024 International Conference on

Microwave and Millimeter Wave Technology (ICMMT), Beijing, China, 16 May 2025; pp. 1–3. [CrossRef]
21. Nimbolkar, A.; Kumar, H.; Kumar, G. Alternatives to Metamaterial Based Antennas for Gain and Bandwidth Enhancement. *IETE J. Res.* **2021**, *69*, 1–7. [CrossRef]
22. Ram, D.; Singh, A.K.; Bhattacharyya, S. An Inverted F-Shaped Slotted Broadband Metasurface-Based Circularly Polarized Patch Antenna for 5G Application. *AEU Int. J. Electron. Commun.* **2024**, *187*, 155507. [CrossRef]
23. Fitra, M.; Adam, I.; Yasin, M.N.M.; et al. Miniaturization of Stacked Wearable Antenna for 5G Applications. *J. Teknol.* **2024**, *86*, 137–144. [CrossRef]
24. Asri, A.F.; Mohd Ariff, M.H.; Abas, M.F.; et al. X-Slot Microstrip Patch Antenna for Sub-6 GHz 5G Router Applications. In Proceedings of the 2025 IEEE 8th International Conference on Electrical, Control and Computer Engineering (InECCE), Kuantan, Malaysia, 27 August 2025; pp. 57–62. [CrossRef]
25. Ram, D.; Singh, A.K.; Bhattacharyya, S. A Broadband Gain-Enhanced Metasurface-Based Circularly Polarized Patch Antenna for WLAN Application. *Radio Sci.* **2025**, *60*, 1–13. [CrossRef]
26. Infant, L.S.; Mary, G.A.A.; Mazhar, A.S.; et al. SIW Cavity-Backed Gain-Enhanced Circularly Polarized Metamaterial-Loaded Dual-Band MIMO Antenna for WLAN and 5G Applications. *ACES J.* **2025**, *40*, 363–372. [CrossRef]
27. Shishkin, M.S. Aperture Efficiency Improvement Methods for High-Gain Wideband or Ultrawideband Stacked Microstrip Antennas. In Proceedings of the 2024 IEEE 3rd International Conference on Problems of Informatics, Electronics and Radio Engineering (PIERE), Novosibirsk, Russia, 15 November 2024; pp. 260–265. [CrossRef]
28. Saxena, S.; Nandwani, R.; Mahajan, M.B.; et al. Challenges in Design and Realization of Fabry-Perot Cavity Based High Gain Antennas. In Proceedings of the 2023 IEEE Microwaves, Antennas, and Propagation Conference (MAPCON), Ahmedabad, India, 11 December 2023; pp. 1–4. [CrossRef]
29. Tubbal, F.; Matekovits, L.; Raad, R. Antenna Designs for 5G, IoT and Space Applications. *Electronics* **2022**, *11*, 2484. [CrossRef]
30. Gong, R.; Liu, Y.; Jia, Y. A Design of Wideband Conformal Discone Antenna. In Proceedings of the 2024 International Applied Computational Electromagnetics Society Symposium (ACES-China), Xi'an, China, 16 August 2024; pp. 1–3. [CrossRef]